Pressure-induced phase transitions in the topological crystalline insulator SnTe and its comparison with semiconducting SnSe: Raman and first-principles studies

Sukanya Pal,[1,*] Raagya Arora,[2,*] Subhajit Roychowdhury,[3] Luminita Harnagea,[4] Kumar Saurabh,[4] Sandhya Shenoy,[2] D. V. S. Muthu,[1] Kanishka Biswas,[3] U. V. Waghmare,[2] and A. K. Sood[1,†]

[1]*Department of Physics, Indian Institute of Science, Bangalore 560012, India*

[2]*Theoretical Sciences Unit, Jawaharlal Nehru Center for Advanced Scientific Research, Jakkur P.O., Bangalore 560064, India*

[3]*New Chemistry Unit, Jawaharlal Nehru Center for Advanced Scientific Research, Jakkur P.O., Bangalore 560064, India*

[4]*Department of Physics, Indian Institute of Science Education and Research, Pune 411008, India*

(Received 24 July 2019; accepted 18 March 2020; published 10 April 2020)

SnTe is a narrow band-gap topological crystalline insulator (TCI), whereas SnSe is a normal semiconductor. We report Raman study of SnTe and SnSe as a function of pressure at room temperature along with first-principles density functional theory calculations. Under pressure, isostructural transition is observed in SnTe, as revealed by the anomalous softening of the strongest Raman mode up to 1.5 GPa, accompanied by an increase in the linewidth. Our first-principles calculations show that the mirror Chern number of SnTe does not change and the TCI phase remains unaffected by pressure. Raman signatures of its phase transition at 1.5 GPa are associated with phonon instability at the Γ point and inversion of the lowest-energy conduction bands. An anomaly in the electron-phonon coupling results in anomalous behavior of the Raman modes at this pressure. Further, SnTe undergoes structural transitions at ∼5.8, ∼12, and ∼18.3 GPa. The 5.8-GPa transition is associated with a structural transition from the ambient cubic ($Fm\bar{3}m$) to orthorhombic (*Pnma*) phase, which is no longer a topological insulator, resulting in a topological phase transition. Above the transition pressure of 12 GPa, another orthorhombic *Pnma*[GeS] phase is stabilized, coexisting with the *Pnma* phase. The reduction in the number of observed Raman modes above ∼18.3 GPa and enthalpy calculations show a transition from orthorhombic (*Pnma*) to a more symmetric cubic ($Pm\bar{3}m$) structure. Our high-pressure study of SnSe, on the other hand, reveals that it undergoes two phase transitions: one from the orthorhombic (*Pnma*) structure to the orthorhombic (*Cmcm*) structure at ∼6.2 GPa and the other at ∼12.9 GPa, in which the *Cmcm* phase undergoes a semimetal to metal transition. Density functional theory calculations capture the contrast in the pressure-dependent behavior of the topological crystalline insulator SnTe and the normal semiconductor SnSe.

DOI: 10.1103/PhysRevB.101.155202

I. INTRODUCTION

Being a topological crystalline insulator (TCI), SnTe, a narrow-gap, group IV-VI semiconductor with a direct band gap of ∼0.3 eV at room temperature [1], has stimulated intense research [2]. Its metallic surface states are protected by the mirror symmetry of the crystal similar to the surface states of Z_2 topological insulators (TIs) protected by time-reversal symmetry [3]. TCIs have multiple surface states associated with particular crystal surfaces, with an even number of Dirac cones in its surface electronic structure and band inversions, in contrast to a Z_2 TI exhibiting an odd number of band inversions. Angle-resolved photoemission spectra have confirmed that SnTe has four Dirac cones in the electronic structure of {100}, {111}, and {110} surfaces in the first surface Brillouin zone [2,4]. TCIs are characterized by a nonzero mirror Chern number, with individual Chern numbers C_{+i} and C_{-i} defined on a mirror-invariant plane. The mirror Chern number [5,6], defined as $n_M = (C_{+i} - C_{-i})/2$, is the topological invariant of a TCI. SnTe is also a "negative band gap" material with ordering of its conduction and valence bands near the Fermi energy inverted compared to normal semiconductors like PbTe [7–10]. Such band inversion takes place near the L points in the Brillouin zone where the valence band maximum has L_6^- symmetry and the conduction band minimum has L_6^+ symmetry. A low-temperature Raman study revealed a phase transition at $T_c \sim 105$ K from an ambient cubic paraelectric ($Fm\bar{3}m$) structure to ferroelectric rhombohedral structure (space group $R\bar{3}m$) which is accompanied by the softening of a phonon mode [11,12] caused by strong coupling between interband electronic transitions mediated by transverse optical phonons.

SnTe exhibits interesting behavior as a function of pressure. A resistivity study showed that its resistance gradually decreases with increasing pressure but at 1.8 GPa increases by ∼200%, followed by a gradual decrease with a further increase in pressure [13]. This transition is also accompanied by a first-order structural phase transition from cubic $Fm\bar{3}m$ to the orthorhombic crystal structure (space group *Pnma*) as revealed by x-ray diffraction [13]. First-principles calculations [14] showed that the direct band gap reduces to zero at 1.5 GPa and then gradually opens up at higher pressures. However, angle dispersive x-ray studies along with first-principles structural calculations later [15] did not report

*Both authors contributed equally to this work.
†asood@iisc.ac.in

a transition at 1.5 GPa and showed that a phase transition from cubic $Fm\bar{3}m$ to the intermediate structures (*Pnma*, *Cmcm*, and GeS type structures) occurs at 4.1 GPa and the transition to the cubic $Pm\bar{3}m$ phase occurs at 18.1 GPa. Further, first-principles calculations showed that the high pressure cubic $Pm\bar{3}m$ phase is superconducting, having a critical temperature of ∼7.5 K, which reduces with pressure [16].

SnSe is a *p*-type IV-VI semiconductor with an indirect band gap of ∼0.9 eV and a direct band gap of ∼1.3 eV [17]. At ambient conditions it has a layered orthorhombic structure with the *Pnma* space group which can be viewed as a distorted NaCl structure. Similar to other IV-VI binary semiconductors like GeSe, SnS, and GeS, SnSe has covalent interaction between the atoms (three neighbors) within the layers. Each layer consists of zigzag double-layer planes of tin and selenium atoms, and these layers are separated by weak van der Waals forces. The center of inversion lies at a point between the double layers [18]. An earlier x-ray diffraction study showed that SnSe does not undergo any structural phase transition up to 34 GPa. There are, however, no results for SnTe in Ref. [19]. Electrical resistivity measurements showed that its electrical resistance decreased at 6.5 GPa, indicating a change in the energy gap of the material [20]. Recent first-principles calculations showed that SnSe transforms from the orthorhombic (*Pnma*) to orthorhombic (*Cmcm*) structure at ∼7 GPa and remains in a semiconducting state in the *Cmcm* phase [21]. On the other hand, a synchrotron x-ray study showed that SnSe has an orthorhombic structure with *Pbnm* symmetry [22] at pressures above 10.5 GPa. Another study based on x-ray diffraction, electrical transport measurements, and first-principles calculations showed that SnSe undergoes an electronic transition from a semiconducting to semimetallic state around 12.6 GPa, accompanied by an orthorhombic to monoclinic structural transition [23].

It is evident that the effects of pressure on the structural and electrical properties of SnTe and SnSe have not been clearly established so far, and our aim in this paper is to investigate the pressure-induced phase transitions of these two semiconductors with different topological signatures using Raman scattering and first-principles calculations.

Our main results reveal a (1) change in isosurfaces of charge densities and band inversion between the two lowest-energy conduction bands of SnTe at 1.5 GPa and (2) a topological phase transition at 5.8 GPa as a result of a change in structural symmetry. (3) Two other phase transitions with a change in crystal and electronic band structures of SnTe are observed at $P = 12$ and 18.3 GPa. In comparison, SnSe does not exhibit any low-pressure transition or any changes in the topological order. It undergoes a structural transition at $P = 6.2$ GPa and a semimetal to metal transition at $P = 12.9$ GPa. A phase diagram in Fig. 1 summarizes the phase transitions in SnTe and SnSe as a function of pressure.

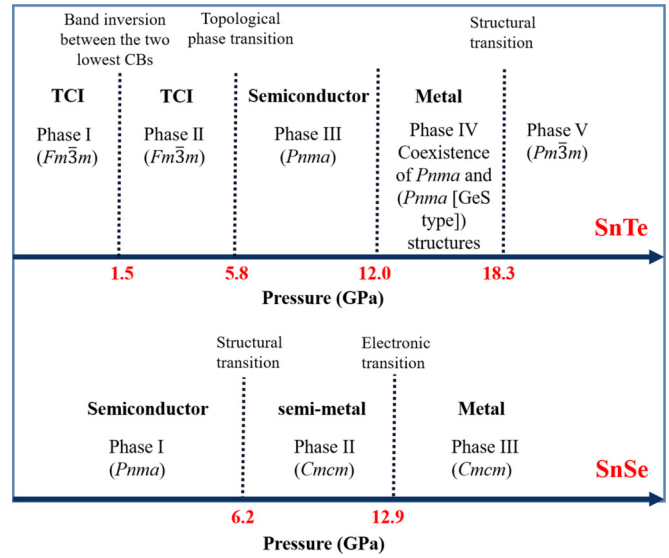

FIG. 1. Phase diagram of SnTe and SnSe at high pressure.

II. EXPERIMENTAL DETAILS

Tin (Alfa Aesar 99.99%+) and tellurium (Alfa Aesar 99.999%+) were used in the synthesis of SnTe crystals without further purification. An ingot (∼7 g) of SnTe was synthesized by mixing the appropriate ratios of high-purity elemental Sn and Te in a quartz tube. The tube was sealed under vacuum (10^{-5} Torr) and slowly heated to 723 K over 12 h, then heated up to 1173 K over 5 h, annealed for 10 h, and slowly cooled down to room temperature over a period of 15 h. The sample was characterized as described in Ref. [24] and confirmed to be in a cubic NaCl structure.

SnSe single crystals were grown using a direct vapor transport technique. Stoichiometric quantities of Sn (shot, 99.999%+, metal basis, Sigma Aldrich) and Se (shot, 99.999%+, metal basis, Alfa Aesar) were loaded in a preheated quartz ampoule inside the glove box. The quartz ampoule, approximately 180 mm in length with a 20-mm inner diameter, containing 8 g of precursors, was sealed under vacuum (10^{-5} Torr) and placed in a horizontal tube furnace under a temperature gradient of −60°C between the extremities. The ampoule was slowly heated to 500 °C, kept there for 10 h, and then heated further to 950 °C, where it was kept for 24 h and then slowly cooled down to 700 °C at a rate of 1.5 °C/h. The ampoule was kept at this temperature for 10 h and then slowly cooled down to room temperature.

High-pressure Raman studies were performed up to 25 GPa at room temperature using a diamond anvil cell (DAC). A very small piece from the bulk crystals (∼50 μm) and a very small ruby chip (∼10 μm) were placed inside a hole in a stainless-steel gasket kept between the two diamonds of a Mao-Bell-type DAC, using a mixture of methanol and ethanol (4:1 ratio) as a pressure-transmitting medium. The ruby fluorescence method [25] was used for pressure calibration. Raman spectra were recorded in a LabRam spectrometer (M/s Horiba) in backscattering geometry, using a 50× objective and laser excitation of 532 nm from a diode-pumped solid-state laser.

III. COMPUTATIONAL METHODS

Our first-principles calculations are within density functional theory (DFT) employing the QUANTUM ESPRESSO (QE) [26] code. To treat the exchange and correlation energy of electrons, we used a generalized gradient approximation (GGA) [27] with a functional parametrized by Perdew, Burke,

and Ernzerhof [28]. The projector augmented wave (PAW) potentials [29] with valence configurations $4d^{10}\ 5s^2\ 5p^2$, $4d^{10}\ 5s^2\ 5p^4$, and $3d^{10}\ 4s^2\ 4p^4$ were adopted for Sn, Te, and Se respectively.

The expansion of wave functions and charge density in the plane wave basis set was truncated with energy cutoffs of 50 and 500 Ry, respectively. The discontinuity in occupation numbers of the electronic states at the Fermi level was smeared with an energy width of $k_BT = 0.005$ Ry in the Fermi-Dirac distribution function. Face-centered cubic ($Fm\bar{3}m$), orthorhombic (*Pnma*, *Pnma*[GeS] type, and *Cmcm*), and cubic ($Pm\bar{3}m$) structures of SnTe were theoretically analyzed to understand the experimentally observed pressure-dependent phase transitions. In calculations of the cubic ($Fm\bar{3}m$) structure of SnTe, Brillouin zone (BZ) integrations were sampled with a uniform mesh of $16 \times 16 \times 16$ k points, while for orthorhombic (*Pnma* and *Cmcm*) and cubic ($Pm\bar{3}m$) unit cells, Brillouin zone (BZ) integrations were sampled with a uniform mesh of $8 \times 8 \times 8$ and $8 \times 10 \times 10$ k points, respectively.

To study the pressure-induced phase transitions in SnSe, its orthorhombic *Pnma* and *Cmcm* structures were analyzed. For *Pnma* structure, wave functions and charge density were represented in plane wave basis sets truncated by cutoff energies of 45 and 400 Ry, respectively, and fixed at 45 and 360 Ry for the *Cmcm* phase. The discontinuity in occupation numbers of electronic states was smeared using a Fermi-Dirac distribution function with broadening of $k_BT = 0.003$ Ry. BZ integrations were sampled on uniform meshes with $8 \times 10 \times 10$ and $10 \times 8 \times 10$ k points in the Brillouin zones of meshes with *Pnma* and *Cmcm* structures, respectively.

To determine the pressure-dependent structure and phonon spectra we used scalar-relativistic PAW potentials to optimize the structure with respect to lattice constants and atomic coordinates through minimization of enthalpy $H = E + PV$ at a given pressure. Lattice dynamical properties were calculated using self-consistent linear response theory within DFT (known as density functional perturbation theory [30]) as implemented in the QE distribution [26].

To obtain phonon dispersion of the $Fm\bar{3}m$ phase of SnTe and of the *Cmcm* phase of SnSe, interatomic force constant matrices were obtained at q vectors on $4 \times 4 \times 4$ and $2 \times 1 \times 1$ meshes, respectively, and dynamical matrices at an arbitrary q vector were obtained using Fourier interpolation. The effects of spin-orbit coupling were included in our calculations of electronic structure through the use of fully relativistic [31] pseudopotentials.

To assess the electronic topology of SnTe, we used the Z2PACK code [32] to determine the Z_2 topological invariant and the mirror Chern number n_M. This involves the use of hybrid Wannier functions [33,34] and employs the idea of time-reversal polarization in calculations of the Z_2 invariants.

IV. RESULTS AND DISCUSSION

A. Experiments

At ambient conditions SnTe crystallizes in the cubic structure (space group $Fm\bar{3}m$), with a lattice constant of 6.3 Å.

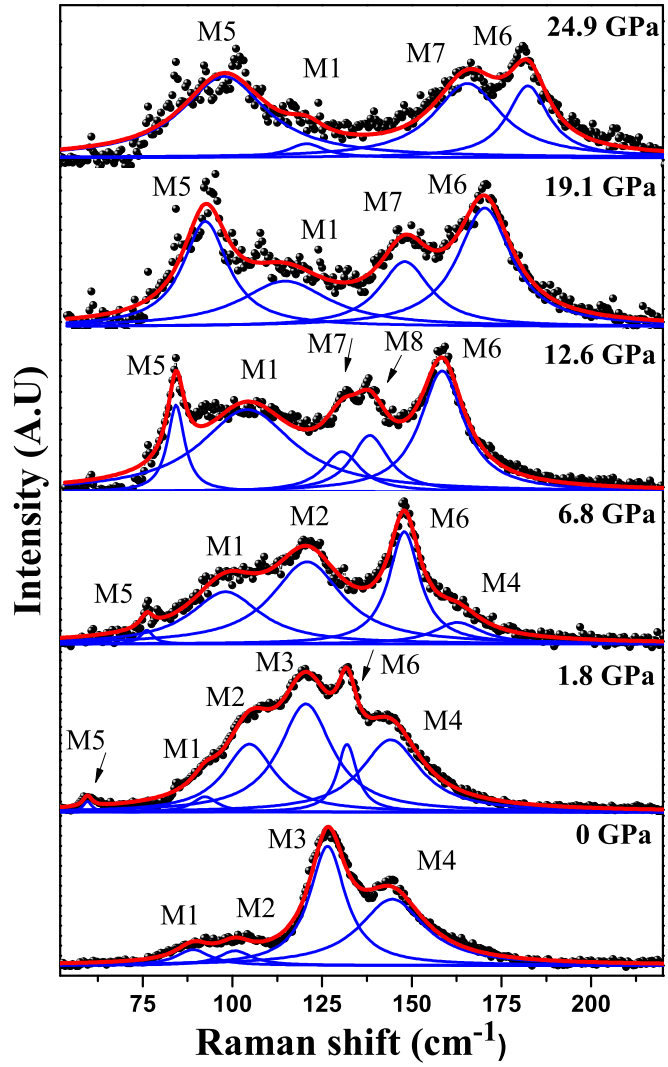

FIG. 2. Raman spectra of SnTe at a few typical pressures in the increasing pressure run. Black solid circles are the experimental data. The solid red lines are the Lorentzian fit to the experimental data points. The blue solid lines are individual fits of the Raman modes. The appearance of new modes is indicated by arrows.

At room temperature, there are no symmetry-allowed, zone-center first-order Raman modes. However, the Raman spectrum at zero pressure inside the DAC (see the bottom panel of Fig. 2) displays four modes at 89.1, 100.8, 126.5, and 144.5 cm^{-1}, marked as M1, M2, M3, and M4, in agreement with an earlier report [11]. We note that in contrast to our results and Ref. [11], Brillson *et al.* [12] did not report these modes at room temperature. We use calculated phonon dispersion see Fig. 7(a) below and one-phonon and two-phonon densities of states [see Fig. 7(b), which will be discussed later] to assign these Raman bands. The first three peaks are disorder-induced first-order Raman modes associated with Brillouin zone optical edge phonons [shown in Fig. 7(a)] at the W (mode M1 and M2) and L points (mode M3), and the broad peak M4 is associated with the two-phonon Raman process [shown in Fig. 7(b)] as supported by theoretical calculations. Figure 2 shows Raman spectra measured at a few typical

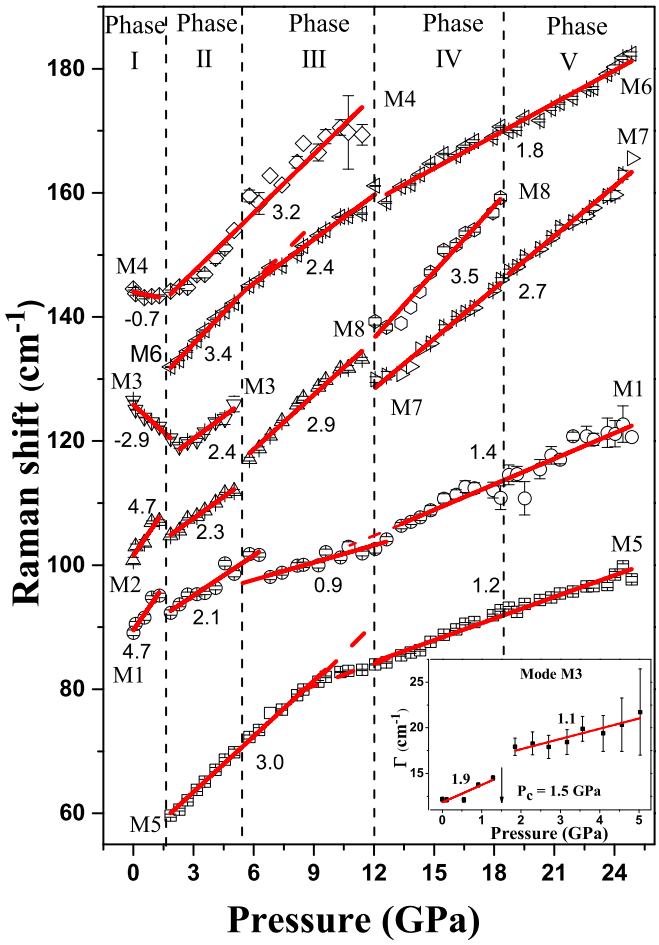

FIG. 3. The Raman shift of SnTe is plotted against applied pressure. Error bars are obtained from the fitting procedure. The solid red lines are the linear fits to the frequencies of the Raman modes. The dashed lines indicate the pressures at which transitions occur. The numbers are the pressure coefficients given by slope $S = d\omega/dP$ (in cm^{-1}/GPa) obtained from linear fits. The inset shows the variation of the FWHM of mode M3 as a function of applied pressure.

pressures in the increasing pressure run at room temperature, and changes in Raman spectra are marked by arrows in the panel showing spectra at 1.8 and 12.6 GPa. The peak positions and full width at half maximum (FWHM) are determined by fitting Lorentzian line shapes after appropriate background corrections. Here the red line represents the composite fit, whereas the blue lines are Lorentzian fits to individual Raman modes. Figure 3 shows the pressure dependence of the mode frequencies of SnTe. Solid lines are linear fits to the data using $\omega_P = \omega_0 + (d\omega/dP)P$, and the values of the slope $S = d\omega/dP$ are given in Fig. 3 as well as listed in Table 1 of the Supplemental Material Ref. [35] along with ω_0 and the corresponding errors. The change in S and appearance of new modes or disappearance of modes with varying pressure indicate possible transitions. Accordingly, the dashed lines mark the phase transitions taking place at ∼1.5, 5.8, 12, and 18.3 GPa.

We observe the following from Fig. 3: (1) Modes M3 and M4 soften until 1.5 GPa (end of phase I), and then the sign of their pressure coefficients changes. (2) The FWHM of M3 (inset) shows a sudden increase at 1.5 GPa. (3) Two new modes marked as M5 and M6 appear at 54.5 and 125.6 cm^{-1}, respectively, at the same pressure. (4) In addition, $|S|$ of both M1 and M2 modes show a change at 1.5 GPa. Our first-principles calculations show that such anomalous behavior of the Raman modes is associated with an optical phonon instability at the Γ point of the Brillouin zone and the anomalous evolution of the electron-phonon coupling through this pressure range. This will be discussed in detail later. (5) The intensity of the strongest mode M3 decreases with increasing pressure, and around 5.8 GPa (end of phase II) it vanishes. Modes M1, M2, and M6 show a change in slope at 5.8 GPa. Enthalpy calculations show that a structural transition from the cubic ($Fm\bar{3}m$) to orthorhombic (*Pnma*) phase takes place at 5.8 GPa. This results in breaking of the mirror symmetry, and the system does not remain a TCI. Our present work is focused on the first two pressure-dependent transitions. We further observe two more phase transitions, as shown in Fig. 3. The change in Raman modes observed at ∼12.0 GPa is associated with the coexistence of orthorhombic *Pnma* and *Pnma*(GeS) structures (which will be discussed later). The anomalies observed at $P \sim 18$ GPa are associated with a structural transition from the orthorhombic (*Pnma*) to cubic ($Pm\bar{3}m$) structure, in agreement with x-ray diffraction results [15], also supported by our enthalpy analysis. Raman spectra were recorded at a few typical pressures in the reverse pressure cycle (see Fig. S1 of the Supplemental Material Ref. [35]), and the pressure dependence of all the Raman modes (see Fig. S2 of the Supplemental Material Ref. [35]) shows that all four transitions (occurring at 17.2, 12.4, 7.2, and 1.9 GPa) are reversible and phase I is recovered at $P \sim$ 1.9 GPa. The Raman spectrum at zero pressure shows that peak positions are shifted from their starting values, showing that transitions are reversible but exhibit a weak hysteresis.

In contrast to SnTe, SnSe has a layered orthorhombic crystal structure at ambient pressure with eight atoms per unit cell and lattice parameters $a = 11.49$ Å, $b = 4.15$ Å, and $c = 4.44$ Å [36]. Sn and Se atoms are in 4c Wyckoff positions $(x, 1/4, z)$. Among the 21 zone center optical phonons, only 12 modes are Raman active ($4A_g + 2B_{1g} + 4B_{2g} + 2B_{3g}$) [18,37].

Figure 4 shows Raman spectra at a few typical pressures in the increasing pressure run at room temperature. The spectrum at zero pressure inside the DAC (see the bottom panel of Fig. 4) displays seven modes: 34.7 cm^{-1} (M1), 72.8 cm^{-1} (M2), 109.2 cm^{-1} (M3), 131.3 cm^{-1} (M4), 153.7 cm^{-1} (M5), 232.1 cm^{-1} (M6), and 291.7 cm^{-1} (M7). Modes M1, M2, M4, and M5 are A_g modes, and M3 is a B_{3g} mode, as shown by previous studies [18,38]. Broad peaks of the M6 and M7 modes can be assigned as second-order Raman modes. Another very weak mode at 188.1 cm^{-1} (M′) observed until 2.5 GPa corresponds to the impurity phase of the $SnSe_2$ phase. Changes in Raman spectra with pressure are clearly seen in Fig. 4, where the arrows mark the appearance of new Raman modes. Figure 5 shows the pressure dependence of the mode frequencies, where solid lines are the linear fit to the data and the pressure coefficients are given in Fig. 5 and listed in Table 2 of the Supplemental Material Ref. [35] along with ω_0 and the corresponding errors. The dashed lines in Fig. 5 mark the transitions taking place at ∼6.2 and 12.9 GPa.

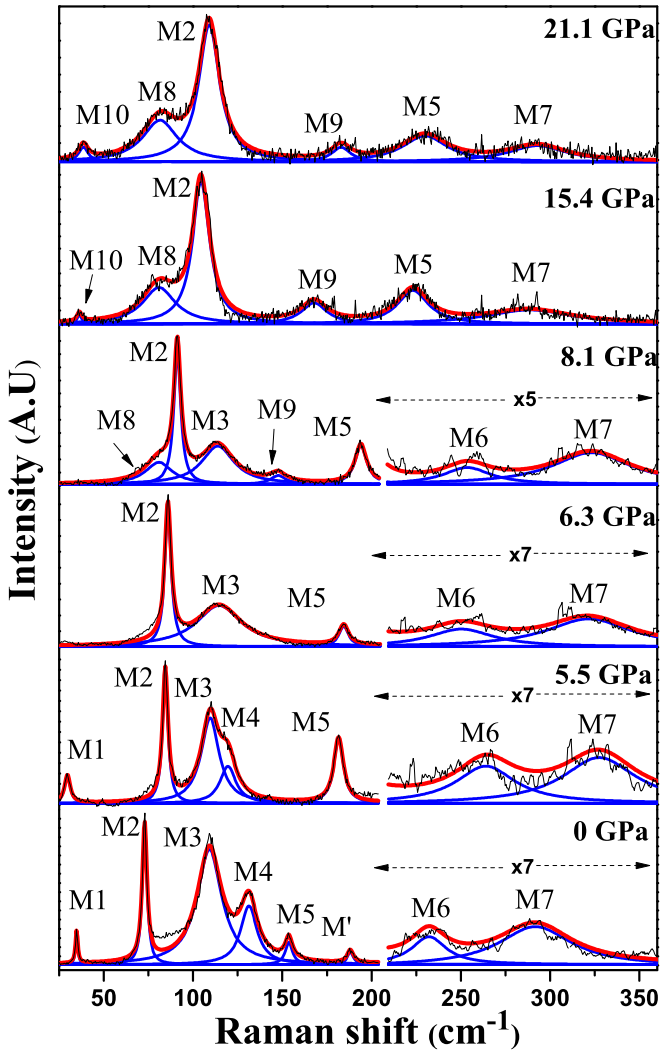

FIG. 4. Raman spectra of SnSe at a few typical pressures in the increasing pressure run. The solid blue lines are the Lorentzian fit to the experimental data given by the black line. The red solid lines are individual fits of the Raman modes. The arrows indicate the appearance of new modes owing to pressure-induced phase transitions.

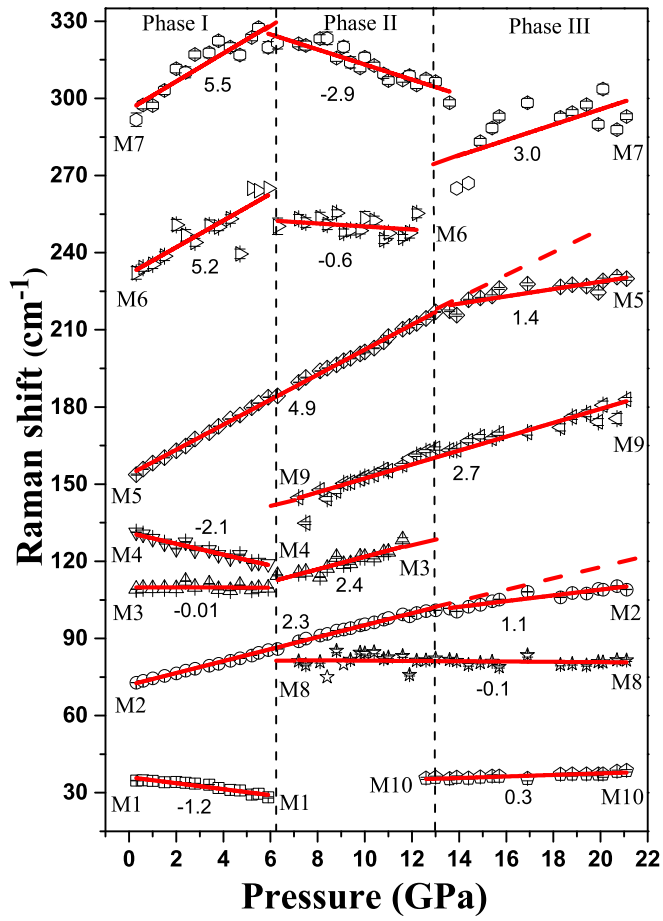

FIG. 5. The Raman shift of SnSe is plotted against applied pressure. The error bars are obtained from the fitting procedure. The solid red lines are the linear fits to the frequencies of the Raman modes. The black dashed lines indicate the pressure where the transitions are taking place. The numbers are the value of the slope $d\omega/dP$ (in $\mathrm{cm}^{-1}/\mathrm{GPa}$) obtained from linear fits.

We make the following observations in Fig. 5: (1) The pressure dependence of the frequencies of modes M1, M3, and M4 are anomalous; that is, frequency decreases with increasing pressure to 6.2 GPa. (2) M4 disappears, and the frequency of M1 softens below the low-frequency cutoff of our Raman spectrometer. (3) The slope S of mode M3 changes its sign. (4) The pressure coefficients of both modes M6 and M7 change significantly. (5) In addition to all these changes, two new modes marked as M8 and M9 at 81.2 and 144.6 cm^{-1}, respectively, appear in the Raman spectra at $P \sim 6.2$ GPa and are observed up to the maximum pressure (21 GPa). This phase transition at 6.2 GPa can be associated with a structural phase transition from the ambient orthorhombic *Pnma* structure to another orthorhombic *Cmcm* structure as deduced from the first-principles calculations [21]. (6) Raman modes M3 and M6 disappear at 12.9 GPa. (7) A new mode, M10, appears at 35.6 cm^{-1} at $P \sim 12.9$ GPa, and also the pressure coefficient $|S|$ of mode M5 decreases significantly. (8) Modes M2 and M7 show a change in the slope S at ∼12.9 GPa. The nature of the second phase transition observed at $P \sim 12.9$ GPa will be discussed later. Raman spectra were recorded in the decreasing pressure cycle (see Fig. S3 of the Supplemental Material Ref. [35]), and the pressure dependence of all the Raman modes (see Fig. S4 of the Supplemental Material Ref. [35]) reveals the two transitions at 12 and 7 GPa, showing the reversible nature.

B. Theoretical calculations

We now present a theoretical analysis to understand the observed pressure-dependent transitions in the TCI SnTe. Our estimate of the optimized lattice constant of the cubic ($Fm\bar{3}m$) phase of SnTe is $a = 6.37$ Å, which is within the typical errors of the GGA calculations relative to its experimental value ($a = 6.32$ Å).

The electronic structure of SnTe calculated with the spin-orbit interaction at the optimized lattice constants gives a direct band gap at the L point of 0.15 eV, compared to its experimental value [1] of 0.3 eV; such underestimation of

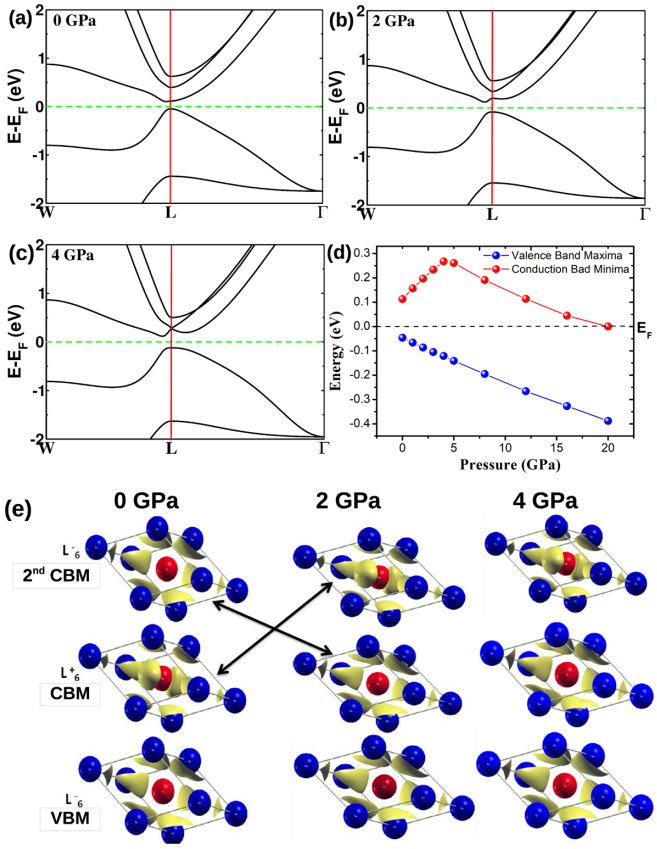

FIG. 6. Electronic structure of the cubic ($Fm\bar{3}$m) phase of SnTe calculated with spin-orbit coupling at (a) 0 GPa, (b) 2 GPa, and (c) 4 GPa and (d) the variation in the VBM and CBM with pressure at the L point of the Brillouin zone. (e) Isosurfaces of charge densities associated with electronic states at the VBM, CBM, and second conduction band minimum at the L point below (a) and above (b), the critical pressure revealing the inversion of the lowest two conduction bands at this transition.

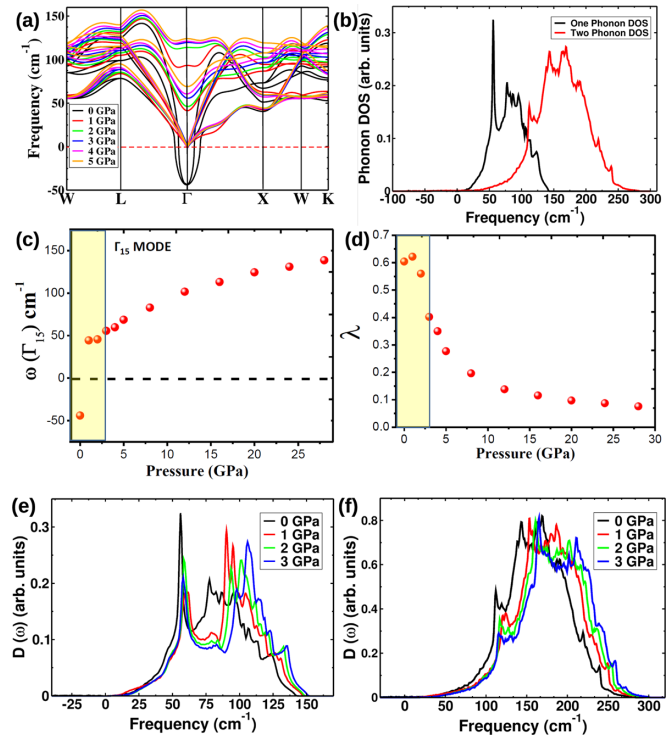

FIG. 7. (a) Calculated phonon dispersion of the cubic ($Fm\bar{3}$m) structure of SnTe at pressures ranging from 0 to 5 GPa, exhibiting imaginary phonon frequencies depicting the instability of cubic structure at $P = 0$ GPa. (b) One- and two-phonon densities of states of cubic SnTe at 0 GPa. (c) Calculated frequency ω of the optical phonon (Γ_{15}) at the Γ point as a function of pressure, showing an anomaly at low pressures, and (d) its electron-phonon coupling. Evolution of (e) the one-phonon DOS and (f) two-phonon DOS with hydrostatic pressure changing from 0 to 3 GPa.

the band gaps is typical of DFT. With increasing hydrostatic pressure, the conduction band minimum (CBM) and valence band maximum (VBM) at the L point move away from each other, and the band gap increases [Figs. 6(a) to 6(c)]. The band gap at the L point increases from 0.15 eV at 0 GPa to 0.4 eV at 5 GPa [Fig. 6(d)]. A close examination of the electronic structure near the L point [Fig. 6(a) and 6(b)] reveals a crossing of the two conduction bands as pressure changes from 0 to 2 GPa. The inversion of bands at the CBM and second CBM at L is evident from the isosurfaces of charge densities [Fig. 6(e)] associated with these conduction bands. Such band inversion is often an indicator of the electronic topological transition (ETT) in materials and hence motivates us to check the bulk electronic topology of SnTe. Symmetry analysis shows that the parities of the electronic wave functions at the CBM and second CBM are L_6^+ and L_6^-. To proceed with the symmetry-based arguments, we determined the Z_2 topological index using a robust and more definitive method as implemented in the Z2PACK code. The calculated Z_2 topological invariant ν_0 of SnTe remains zero before and after the band inversion, confirming no change in its electronic topology and establishing the trivial band topology of SnTe with respect to Z_2. In SnTe, there could be a change in electronic topology with respect to the TCI nature, as SnTe is a topological crystalline insulator at ambient conditions. We study the evolution of the mirror Chern numbers n_M as a function of pressure. The mirror Chern numbers n_M of SnTe calculated at 0 and 2 GPa are $n_M = 2$, confirming the robust nontrivial TCI phase of SnTe at 2 GPa.

To probe this further, we monitored the effects of hydrostatic pressure on zone center (Γ point) optical phonons. A compression of the unit cell leads to hardening of all the three degenerate optical Γ_{15} modes [Fig. 7(a)], which is evident in the phonon density of states [Fig. 7(b)]. Upon application of hydrostatic pressure, the Γ point instability at $\omega \sim 43i$ cm^{-1} vanishes, and a stable structure is obtained at $P \geqslant 1$ GPa that exhibits a Γ point optical mode frequency of 40 cm $^{-1}$. The anomalous behavior of these optical phonon modes with pressure from 0 to 2 GPa [Fig. 7(c)] corroborates the experimentally observed changes in Raman spectra at 1.5 GPa. The concurrent anomalous evolution of the electron-phonon coupling of this optical phonon (Γ_{15}) with pressure across the critical pressure [see Fig. 7(d)] further validates the subtle Raman changes observed at low pressure.

To investigate the pressure-dependent structural phase transition from the cubic ($Fm\bar{3}m$) to orthorhombic [*Pnma*, *Pnma* (GeS type), *Cmcm*] phases, we estimated the changes

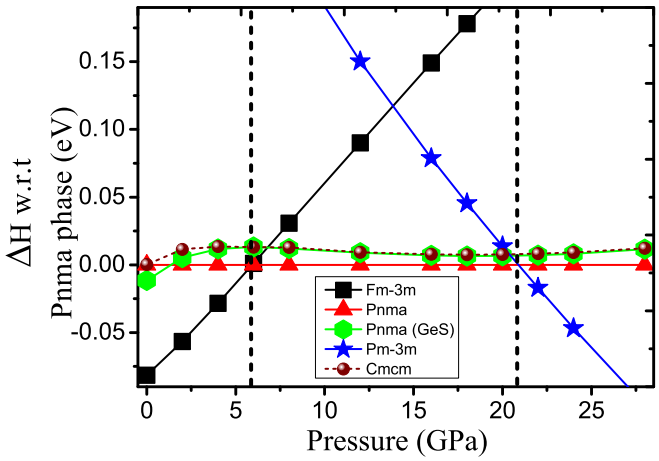

FIG. 8. Pressure-dependent enthalpy ΔH of cubic $Fm\bar{3}m$, orthorhombic *Pnma* (GeS), *Cmcm*, and cubic $Pm\bar{3}m$ phases of SnTe relative to the orthorhombic *Pnma* phase.

in enthalpy ΔH of these structures. Figure 8 shows that ΔH of the cubic structure with respect to the orthorhombic (*Pnma*) phase increases monotonically with pressure and attains a positive value at ∼5.8 GPa, confirming a cubic ($Fm\bar{3}m$) to orthorhombic (*Pnma*) structural phase transition and thus correlating with the experimentally observed Raman changes at 5.8 GPa. Further, we find that the orthorhombic *Pnma* structure of SnTe remains stable up to 21 GPa.

To explore the possibility of the experimentally observed 12-GPa phase transition, electronic structures of orthorhombic *Pnma* and *Pnma* (GeS type) phases have been calculated. Here, we examine the electronic properties of these polymorphs of SnTe in the intermediate-pressure range (see Figs. S5 and S6 in the Supplemental Material Ref. [35]). At 6 GPa, the electronic structure shows that the overlap between the conduction and valence bands makes the *Pnma* (GeS type) structure metallic [see Fig. S6(a) in the Supplemental Material Ref. [35]], while *Pnma* is a zero-band-gap semiconductor [see Fig. S5(a) in the Supplemental Material Ref. [35]]. With increasing hydrostatic pressure the valence bands and conduction bands of the *Pnma* phase cross the Fermi level, and at $P = 8$ GPa [Fig. 9(a)] the metallization of the *Pnma* phase is achieved, through an indirect band gap closure along the X-Γ-Z directions. In addition, the VBM at the T point crosses the Fermi level at a pressure of ∼11 GPa [Fig. 9(b)]. Figure 9(c) shows the first Brillouin zone along with the high-symmetry points used in our calculations. With increasing hydrostatic pressure the enhanced metallic behavior of the *Pnma* phase is also evident from the increased density of states at the Fermi level. Although the *Pnma* (GeS type) phase remains metallic throughout the range of intermediate pressures [see Figs. S6(a) to S6(d) in the Supplemental Material Ref. [35]], it shows an enhanced density of states at the Fermi level with increasing pressures. This is attributed to the additional contribution of valence bands along the UX direction near E_F and additional valence bands crossing the Fermi level along the XS direction at ∼13 GPa [see Fig. S6(e) in the Supplemental Material Ref. [35]].

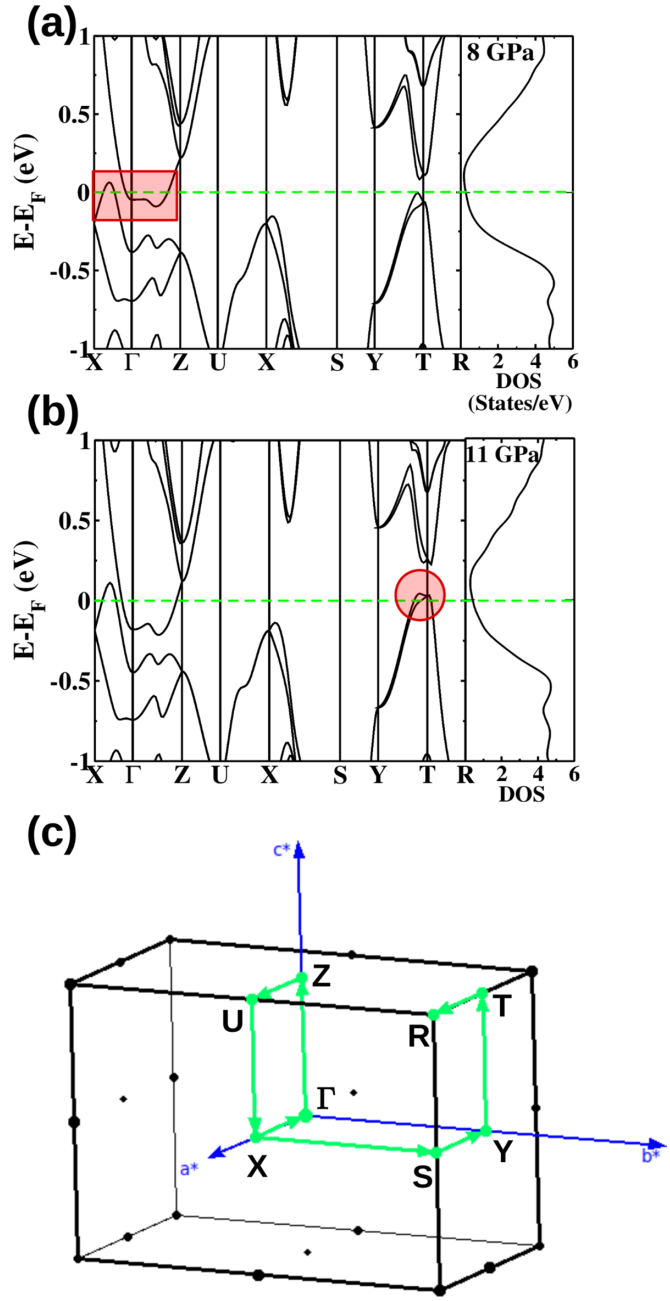

FIG. 9. Electronic structures of the orthorhombic (*Pnma*) structure of SnTe at (a) $P = 8$ GPa and (b) 11 GPa are calculated with the inclusion of the effects of the spin-orbit coupling and corresponding electronic density of states, showing enhanced metallicity with increasing pressure. (c) The first Brillouin zones with high-symmetry points used in calculations. The red shaded region within the square indicates the metallization of the *Pnma* phase at 8 GPa. The shaded region within the red circle indicates the Fermi energy crossing of the VBM at the T point at 11 GPa. The electronic structure at 6, 12, 13, and 16 GPa is given in the Supplemental Material Ref. [35].

However, these electronic structure calculations are not sufficient to support the experimentally observed phase transition at ∼12 GPa.

To explore this phase transition further, we analyze Γ point phonons of orthorhombic *Pnma* and *Pnma* (GeS) structures.

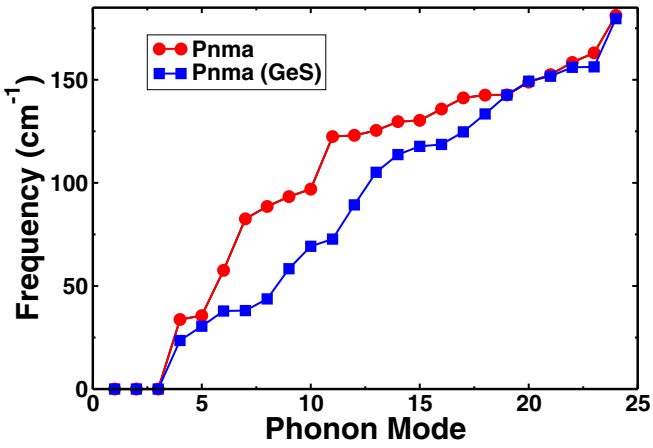

FIG. 10. Frequencies of the zone center (Γ) point phonons of the *Pnma* and *Pnma* (GeS type) phases are plotted. The x axis depicts the mode number, and the y axis depicts the respective frequencies. At 16 GPa the optical phonon modes of the *Pnma* (GeS) phase are notably softer in comparison to the *Pnma* phase.

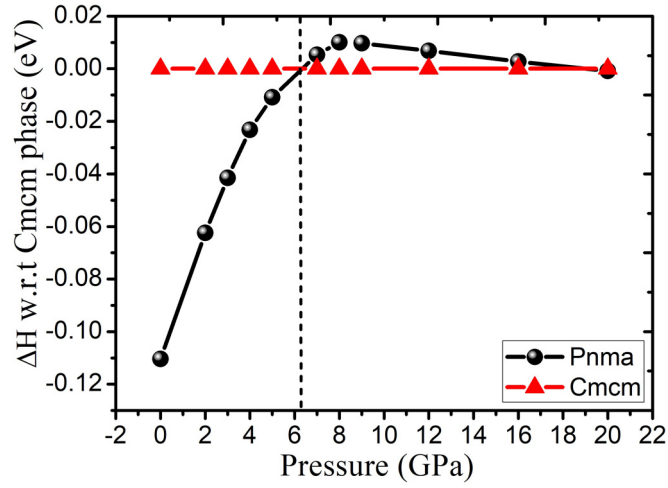

FIG. 11. Pressure-dependent enthalpy ΔH of the orthorhombic *Pnma* phase of SnSe relative to the orthorhombic *Cmcm* phase, demonstrating a structural phase transition from the *Pnma* to *Cmcm* phase at $P = 6.3$ GPa.

At the Γ point there are 3 acoustic and 21 optical (8 atoms in the unit cell) phonon modes. All 24 Γ mode frequencies are plotted in Fig. 10. At 16 GPa, the *Pnma* (GeS) phase exhibits Γ point phonon modes softer than those of the *Pnma* phase (Fig. 10). The observed evolution of Raman modes across the transition pressure of ∼12 GPa also points to a similar trend (see Table 1 of the Supplemental Material Ref. [35]). We therefore attribute the experimentally observed Raman changes in SnTe at 12 GPa to the coexistence of orthorhombic *Pnma* (GeS) and *Pnma* structures. The presence of the *Pnma* (GeS) phase above 12-GPa pressure thus results in lower-frequency phonon modes. The difference in enthalpy of the *Pnma* and *Pnma* (GeS) phases (Fig. 8) decreases from ∼13 to ∼7 meV on moving from 8 to 16 GPa, hinting within the computational errors at the possibility of their coexistence at $P > 12$ GPa, correlating with experimentally observed Raman changes. To analyze the pressure-dependent phase transition from the *Pnma* to cubic ($Pm\bar{3}m$) phase, we obtained the changes in enthalpy of these structures and found a phase transition from the orthorhombic *Pnma* phase to the cubic phase at 21 GPa (Fig. 8), which correlates with the experimental P_c of 18.3 GPa.

We now discuss our theoretical results on SnSe, revealing phase transitions at 6.2 and 12.9 GPa. At ambient conditions SnSe has a layered orthorhombic crystal structure with the *Pnma* space group having eight atoms per unit cell, and experimental lattice parameters are $a = 11.50$ Å, $b = 4.15$ Å, and $c = 4.44$ Å, in agreement with an earlier report [36]. In comparison, our calculated values are $a = 11.77$ Å, $b = 4.22$ Å, and $c = 4.53$ Å and are close to the experimental values. To investigate the pressure-dependent structural phase transition to the orthorhombic (*Cmcm*) phase, we estimated changes in enthalpies ΔH of the orthorhombic *Cmcm* and *Pnma* phases of SnSe. ΔH of the *Pnma* structure increases with pressure and attains a positive value at ∼6.3 GPa (Fig. 11), establishing a structural phase transition from the *Pnma* to *Cmcm* structure correlating with the observed Raman anomalies at 6.2 GPa.

The electronic structure of orthorhombic *Pnma* SnSe calculated while including the spin-orbit interaction at the optimized lattice constant reveals an indirect band gap of 0.7 eV. Our estimate of its band gap is slightly lower than the experimental band gap of ∼0.9 eV [17]. Under compression, both VBM and CBM gradually move towards the Fermi level, and the energy band gap reduces from 0.7 to ∼0.1 eV at 6 GPa [Figs. 12(a) and 12(b)]. A detailed electronic structure along the full path and all pressures are given in the Supplemental Material (see Fig. S7, Ref. [35]). Our calculated lattice parameters of the *Cmcm* structure of SnSe are $a = b = 4.29$ Å and $c = 11.93$ Å, which compare well with experiments [39] (*Cmcm*: $a, c = 4.31$ Å, $b = 11.70$ Å). With increasing hydrostatic pressure (starting from 7 GPa), the electronic structure evolves to a semimetallic *Cmcm* phase of SnSe, with the crossing of the VBM and CBMs occurring at $P = 7$ GPa [see Fig. S8(a) in the Supplemental Material Ref. [35]]. To probe the experimentally observed transition at 13 GPa, we examine the band structure and phonons for *Cmcm* phases [as shown in Figs. 13(a) to 13(c)]. Figure 13(d) shows the first Brillouin

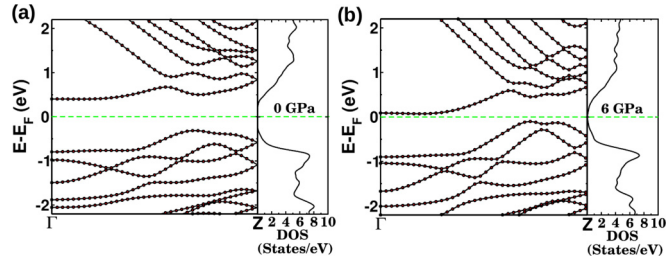

FIG. 12. Electronic structure of the orthorhombic (*Pnma*) structure of SnSe at (a) $P = 0$ GPa and (d) 6 GPa calculated with the inclusion of effects of the spin-orbit coupling and corresponding electronic density of states, showing an enhanced density of states at the Fermi level with increasing pressure. The electronic structure along the full path and at intermediate pressures is given in the Supplemental Material Ref. [35].

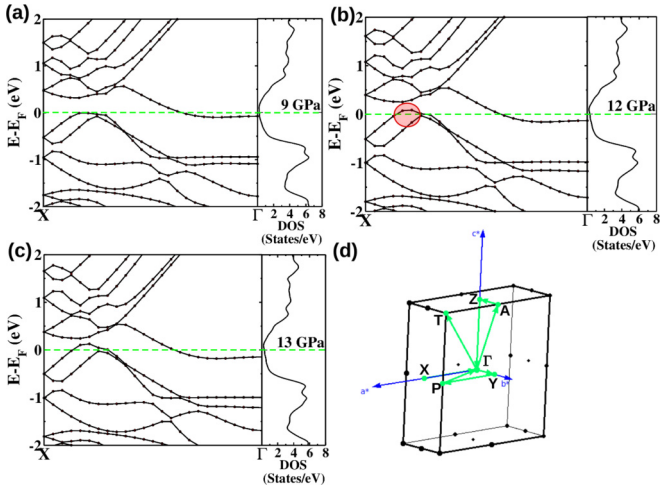

FIG. 13. Electronic structure and corresponding electronic density of states of the orthorhombic (*Cmcm*) structure of SnSe at (a) 9 GPa, (b) 12 GPa, and (c) 13 GPa calculated with the inclusion of spin-orbit coupling. (d) The first Brillouin zones with high-symmetry points used in the calculations. The shaded region within the red circle indicates the Fermi level crossing of valence bands at ∼12 GPa along the Γ*X* direction. The electronic structure along the full path and at various other pressures is given in Supplemental Material Ref. [35].

zone marked by the high-symmetry points used in our calculations. The *Cmcm* phase shows an enhanced electronic density of states at the Fermi level with increasing pressure. This is attributed to the additional contribution of conduction bands at the Fermi level with increasing hydrostatic pressure and valence bands along the Γ*X* direction crossing the Fermi level at ∼12 GPa [Fig. 13(b)].

Consequently, the *Cmcm* phase of SnSe undergoes a semimetal to metal transition at $P \sim 12$ GPa. Phonons of the *Cmcm* phase along the Γ*X* direction reveal an instability at 9 GPa (see Fig. S9 in the Supplemental Material Ref. [35]). On compression, the instability reduces, and a stable structure exhibiting no imaginary frequencies is obtained at 16 GPa (see Fig. S9 in the Supplemental Material Ref. [35]). The transition observed at ∼12.9 GPa in experiment is thus identified as a semimetal to metal transition (occurring at 12 GPa in our calculations).

V. CONCLUSIONS

In summary, combining Raman measurements and first-principles density functional theoretical calculations for the TCI SnTe reveals that at ∼1.5 GPa, a band inversion takes place among the lowest-energy conduction bands, although there is no change in the mirror Chern number in the system, confirming the robust nontrivial TCI phase of SnTe. The observed transition at 5.8 GPa is associated with the cubic ($Fm\bar{3}m$) to orthorhombic (*Pnma*) structural phase transition, which results in breaking the mirror symmetry and a topological phase transition. The ∼12-GPa transition is marked as the onset of the coexistence of the orthorhombic *Pnma* and *Pnma* (GeS) phases. Another structural transition observed at $P \sim 18.3$ GPa transforms SnTe to a more symmetric cubic ($Pm\bar{3}m$) structure. On the other hand, SnSe, a normal semiconductor, does not show the low-pressure transition at 1.5 GPa but undergoes a pressure-induced structural phase transition at $P \sim 6.2$ GPa, marked by the disappearance of Raman modes, transforming SnSe from an orthorhombic *Pnma* structure to another more symmetric orthorhombic *Cmcm* structure, in agreement with our theoretical analysis. Another phase transition at $P \sim 12.9$ GPa is correlated with the semimetal to metal transition of the *Cmcm* phase. We hope that our results will motivate studies for discovering materials which are TCIs as a result of doping (like in $Pb_{1-x}Sn_xTe$) or internal chemical pressure.

ACKNOWLEDGMENTS

A.K.S. acknowledges funding from the Department of Science and Technology (DST), India. S.P. acknowledges DST for an Inspire Fellowship. S.R. acknowledges the Council of Scientific and Industrial Research (CSIR) for a fellowship. L.H. acknowledges DST, India [Grant No. SR/WOS-A/PM-33/2018 (G)], for funding support and Dr. S. Singh for allowing the use of the crystal growth facilities in his laboratory. U.V.W. acknowledges support from a J. C. Bose National Fellowship, a Sheikh Saqr Fellowship, and a project funded by IKST.

[1] L. Esaki and P. J. Stiles, Phys. Rev. Lett. **16**, 1108 (1966).
[2] Y. Tanaka, Z. Ren, T. Sato, K. Nakayama, S. Souma, T. Takahashi, K. Segawa, and Y. Ando, Nat. Phys. **8**, 800 (2012).
[3] T. H. Hsieh, H. Lin, J. Liu, W. Duan, A. Bansil, and L. Fu, Nat Commun. **3**, 982 (2012).
[4] J. Liu, W. Duan, and L. Fu, Phys. Rev. B **88**, 241303(R) (2013).
[5] J. C. Y. Teo, L. Fu, and C. L. Kane, Phys. Rev. B **78**, 045426 (2008).
[6] L. Fu, Phys. Rev. Lett. **106**, 106802 (2011).
[7] S. Rabii, Phys. Rev. **182**, 821 (1969).
[8] J. O. Dimmock, I. Melngailis, and A. J. Strauss, Phys. Rev. Lett. **16**, 1193 (1966).
[9] Y. W. Tung and M. L. Cohen, Phys. Rev. **180**, 823 (1969).
[10] J. S. Melvin and D. C. Hendry, J. Phys. C **12**, 3003 (1979).
[11] S. Sugai, K. Murase, and H. Kawamura, Solid State Commun. **23**, 127 (1977).
[12] L. J. Brillson, E. Burstein, and L. Muldawer, Phys. Rev. B **9**, 1547 (1974).
[13] J. A. Kafalas and A. N. Mariano, Science **143**, 952 (1964).
[14] W. Li, Q. Y. He, J. F. Chen, Z. L. Pan, and T. Wang, Chem. Phys. Lett. **616–617**, 196 (2014).
[15] D. Zhou, Q. Li, Y. Ma, Q. Cui, and C. Chen, J. Phys. Chem. C **117**, 5352 (2013).
[16] D. Zhou, Q. Li, Y. Ma, Q. Cui, and C. Chen, J. Phys. Chem. C **117**, 12266 (2013).

[17] I. Lefebvre, M. A. Szymanski, J. Olivier-Fourcade, and J. C. Jumas, Phys. Rev. B **58**, 1896 (1998).
[18] H. R. Chandrasekhar, R. G. Humphreys, U. Zwick, and M. Cardona, Phys. Rev. B **15**, 2177 (1977).
[19] T. Chattopadhyay, A. Werner, H. G. von Schnering, and J. Pannetier, Rev. Phys. Appl. **19**, 807 (1984).
[20] A. Agarwal, P. H. Trivedi, and D. Lakshminarayana, Cryst. Res. Technol. **40**, 789 (2005).
[21] S. Alptekin, J. Mol. Model. **17**, 2989 (2011).
[22] I. Loa, R. J. Husband, R. A. Downie, S. R. Popuri, and J.-W. G. Bos, J. Phys.: Condens. Matter **27**, 072202 (2015).
[23] J. Yan, F. Ke, C. Liu, L. Wang, Q. Wang, J. Zhang, G. Li, Y. Han, Y. Ma, and C. Gao, Phys. Chem. Chem. Phys. **18**, 5012 (2016).
[24] S. Roychowdhury, U. S. Shenoy, U. V. Waghmare, and K. Biswas, J. Mater. Chem. C **5**, 5737 (2017).
[25] H. K. Mao, J. Xu, and P. M. Bell, J. Geophys. Res. **91**, 4673 (1986).
[26] QUANTUM ESPRESSO is a community project for high-quality quantum-simulation software based on density functional theory and coordinated by P. Giannozzi. See http://www.quantum-espresso.org.
[27] X. Hua, X. Chen, and W. A. Goddard, III, Phys. Rev. B **55**, 16103 (1997).
[28] J. P. Perdew, K. Burke, and M. Ernzerhof, Phys. Rev. Lett. **77**, 3865 (1996).
[29] G. Kresse and D. Joubert, Phys. Rev. B **59**, 1758 (1999).
[30] S. Baroni, S. de Gironcoli, A. Dal Corso, and P. Giannozzi, Rev. Mod. Phys. **73**, 515 (2001).
[31] A. Dal Corso, Comput. Mater. Sci. **95**, 337 (2014).
[32] D. Gresch, G. Autès, O. V. Yazyev, M. Troyer, D. Vanderbilt, B. A. Bernevig, and A. A. Soluyanov, Phys. Rev. B **95**, 075146 (2017).
[33] A. A. Soluyanov and D. Vanderbilt, Phys. Rev. B. **83**, 235401 (2011).
[34] J. Bhattacharjee and U. V. Waghmare, Phys. Rev. B **71**, 045106 (2005).
[35] See Supplemental Material at http://link.aps.org/supplemental/10.1103/PhysRevB.101.155202 for (1) Raman spectra and pressure dependence of the Raman modes in the decreasing pressure cycle of the two samples, (2) Tabular list of the extracted experimental parameters of the two samples in the increasing pressure cycles, and (3) Theoretically obtained electronic structures, density of states and phonon dispersion of different phases at different pressures of the samples.
[36] M. Sist, J. Zhang, and B. B. Iversen, Acta Crystallogr. B **72**, 310 (2016).
[37] T. Fukunaga, S. Sugai, T. Kinosada, and K. Murase, Solid State Commun. **38**, 1049 (1981).
[38] J. Zhang, H. Zhu, X. Wu, H. Cui, D. Li, J. Jiang, C. Gao, Q. Wang, and Q. Cui, Nanoscale **7**, 10807 (2015).
[39] T. Chattopadhyay, J. Pannetier, and H. G. Vonschnering, J. Phys. Chem. Solids **47**, 879 (1986).